

Solid-state infrared-to-visible upconversion sensitized by colloidal nanocrystals

Mengfei Wu[†], Daniel N. Congreve[†], Mark W. B. Wilson[†], Joel Jean, Nadav Geva, Matthew Welborn, Troy Van Voorhis, Vladimir Bulović^{*}, Mounji G. Bawendi^{*} and Marc A. Baldo^{*}

Optical upconversion via sensitized triplet-triplet exciton annihilation converts incoherent low-energy photons to shorter wavelengths under modest excitation intensities¹⁻³. Here, we report a solid-state thin film for infrared-to-visible upconversion that employs lead sulphide colloidal nanocrystals as a sensitizer. Upconversion is achieved from pump wavelengths beyond $\lambda = 1 \mu\text{m}$ to emission at $\lambda = 612 \text{ nm}$. When excited at $\lambda = 808 \text{ nm}$, two excitons in the sensitizer are converted to one higher-energy state in the emitter at a yield of $1.2 \pm 0.2\%$. Peak efficiency is attained at an absorbed intensity equivalent to less than one sun. We demonstrate that colloidal nanocrystals are an attractive alternative to existing molecular sensitizers, given their small exchange splitting, wide wavelength tunability, broadband infrared absorption, and our transient observations of efficient energy transfer. This solid-state architecture for upconversion may prove useful for enhancing the capabilities of solar cells and photodetectors.

Optical upconversion is a process that converts two or more low-energy photons into a single high-energy photon. It has many applications, including biological imaging, night vision, multi-dimensional displays, and photovoltaics⁴. In photovoltaic applications specifically, an optical upconversion layer can capture sub-bandgap photons, increasing the efficiency of a conventional single-junction device beyond the Shockley–Queisser limit⁵.

To upconvert incoherent light at relatively low intensities, it is advantageous to first store the input energy in the form of a long-lived atomic or molecular excited state^{4,6}. Then, a higher energy state can be reached through energy transfer or subsequent absorption. Triplet–triplet annihilation (TTA) follows this model¹⁻³. However, as energy is stored in molecular triplet excitons that are typically dark and inefficiently created by direct optical excitation, TTA requires a sensitizer to absorb incident light. The sensitizer, typically an organometallic complex¹, forms an excited spin-singlet state, which is then converted to a spin-triplet state through intersystem crossing. Energy is transferred from the excited triplet state of the sensitizer to a triplet state of the annihilator. A pair of triplets on separate annihilator molecules can then undergo TTA to form a single higher-energy singlet exciton.

Despite feasibility at sub-solar irradiance⁷ and internal quantum efficiencies as high as 32% for green-to-blue conversion⁸, demonstrations of infrared-to-visible upconversion via TTA sensitized by organic molecules have been limited to incident wavelengths shorter than $\lambda = 830 \text{ nm}$ ⁹, precluding their application in a variety of solar cell technologies, including crystalline silicon. This is due to the limited number of effective molecular sensitizers in the infrared, which is caused by the exponential increase in non-radiative losses in sensitizers with smaller energy gaps¹⁰. Further, with organometallic sensitizers, there is typically an energy loss of hundreds

of meV during intersystem crossing due to the exchange splitting between sensitizer singlet and triplet states³. Finally, despite efforts to develop TTA-based solid-state upconverters¹¹⁻¹⁴, most demonstrations so far have been in solution, while solar and detection applications require a solid-state architecture.

Here, we replace molecular sensitizers with lead sulphide (PbS) colloidal nanocrystals (NCs); see Fig. 1. The bandgap of the NCs is highly tunable, allowing broadband absorption deep into the infrared^{15,16}. The fine-structure splitting of the NCs is also small, comparable to kT at room temperature¹⁷, which minimizes energy loss during sensitization. Indeed, the upconversion of 980 nm light using lead selenide (PbSe) NCs in solution was recently reported¹⁸. Motivated by recent demonstration that triplets generated by singlet exciton fission in thin tetracene films can efficiently transfer to PbS NCs^{19,20}, we adopt a device structure of solid-state thin films, ensuring a high concentration of active species and short diffusion path lengths for optimal energy transfer; see Fig. 1c. Thus, we achieve sensitized upconversion via TTA from beyond $\lambda = 1 \mu\text{m}$ in a solid-state geometry.

We fabricate devices with three sizes of PbS NCs, all with native oleic acid ligands (see Supplementary Information). When cast into thin films, the first excitonic absorption peaks are at $\lambda = 850$, 960, and 1,010 nm respectively. We then thermally evaporate an 80-nm-thick film of rubrene doped with 0.5 vol% dibenzotetraperiflanthene (DBP)²¹ to form a host–guest annihilator–emitter layer that has been employed in organic light-emitting diodes (OLEDs)²² (Fig. 1b,c). Rubrene was chosen as the annihilator as its first excited triplet state is at 1.14 eV²², making it well positioned for infrared sensitization. Calculations indicate that the triplet state in DBP lies $\sim 0.2 \text{ eV}$ higher than that of rubrene²², so DBP is likely to act as an acceptor for singlet excitons only.

To demonstrate energy transfer from the NCs to rubrene, we excite the samples with a $\lambda = 808 \text{ nm}$ continuous-wave laser. Upconversion is apparent as emission from DBP is clearly observed, with the bluest emission peak at $\lambda = 612 \text{ nm}$ (Fig. 2). Control films consisting of only the organics or only the NCs exhibit no visible emission under the same conditions. We also observe that the DBP doping significantly improves device performance—the upconverted photoluminescence (PL) intensity of doped devices is increased 19-fold compared with those with a neat rubrene layer (see Supplementary Information).

To show that PbS NCs sensitize the TTA process over a broad wavelength range extending beyond $\lambda = 1 \mu\text{m}$, we monitor the visible emission from an upconverter sensitized by $\lambda = 1,010 \text{ nm}$ NCs, while sweeping the excitation wavelength. The excitation spectrum in Fig. 2 (purple crosses) agrees well with the absorption spectrum of the NCs. Given that the difference between the optical gap of these NCs and the triplet exciton energy in rubrene is less than

Energy Frontier Research Center for Excitonics, Massachusetts Institute of Technology, Cambridge, MA 02139, USA. [†]These authors contributed equally to this work. *e-mail: bulovic@mit.edu; mgb@mit.edu; baldo@mit.edu

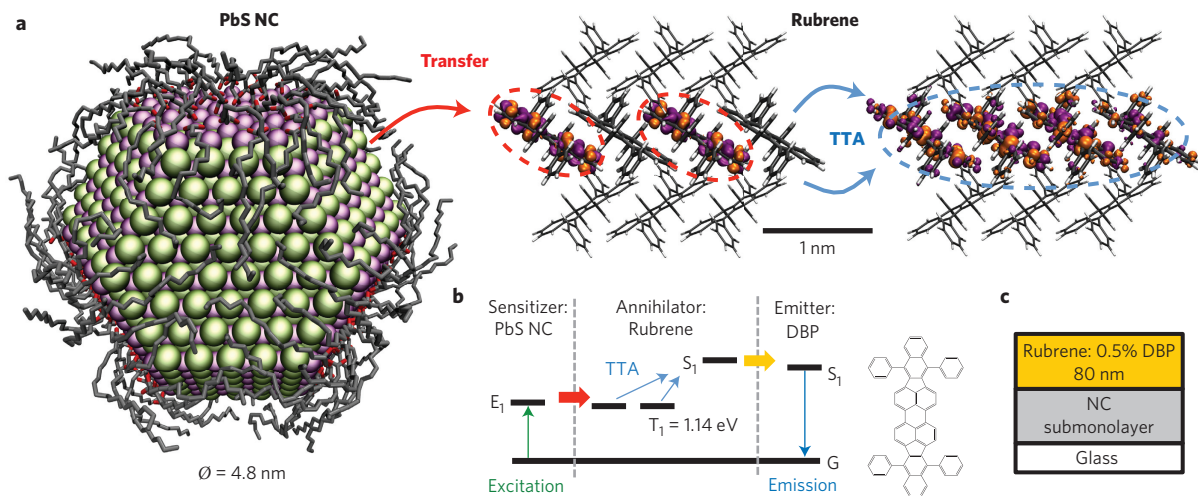


Figure 1 | Schematics of nanocrystal-sensitized upconversion via triplet-triplet annihilation. **a**, PbS colloidal nanocrystals (NCs) absorb incident light and transfer the energy to the triplet state of neighbouring molecular rubrene. If two triplet excitons in rubrene subsequently collide via diffusion, a singlet exciton can be formed. Individual triplet excitons are circled in red, and the larger, delocalized, singlet exciton is circled in blue. **b**, Schematic energy diagram showing the processes of triplet sensitization by the NCs, triplet-triplet annihilation in rubrene and emission from DBP. The addition of the DBP (molecular structure shown) as a guest in the rubrene host increases the fluorescence by a factor of 19. **c**, The solid-state device structure (not to scale).

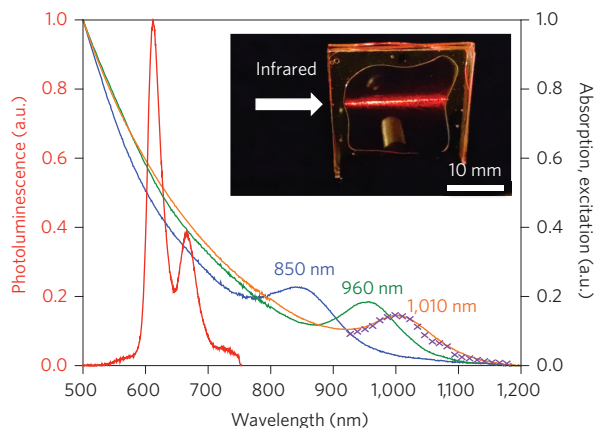


Figure 2 | Absorption, photoluminescence and excitation spectra of infrared upconverter devices. The absorption spectra of the three films of PbS NCs with first excitonic absorption peaks at $\lambda = 850$, 960, and 1,010 nm respectively (right-hand y axis). This is compared with the photoluminescence spectrum of DBP at 0.5 vol% in rubrene (left-hand y axis). Purple crosses indicate the normalized excitation spectrum of DBP at 0.5 vol% in rubrene when sensitized by $\lambda = 1,010$ nm PbS NCs, confirming that upconversion is achieved for pump wavelengths beyond $\lambda = 1 \mu\text{m}$ (right-hand y axis). Inset: photograph showing DBP photoluminescence sensitized by $\lambda = 850$ nm NCs under excitation at $\lambda = 808$ nm.

100 meV, this demonstrates that sensitization can proceed with minimal exothermic drive.

The efficiency of the upconversion process is measured in an integrating sphere²³ using a 91 mW pump laser at $\lambda = 808$ nm, focused to a spot size of approximately $\varnothing = 0.25$ mm and edge-coupled to the glass substrate waveguide, yielding an emissive stripe of dimensions $(0.35 \pm 0.10) \times 20 \text{ mm}^2$ (see inset of Fig. 2). The upconversion quantum efficiency, η , is defined by convention as the fraction of excited states in the sensitizer that are converted to a higher-energy emissive state in the annihilator⁴; see Supplementary Information. For the three sizes of PbS NCs, $\eta_{(850 \text{ nm})} = (1.2 \pm 0.2)\%$, $\eta_{(960 \text{ nm})} = (0.51 \pm 0.07)\%$, $\eta_{(1,010 \text{ nm})} = (0.21 \pm 0.03)\%$, at absorbed optical intensities of (74 ± 21) , (101 ± 29) , and

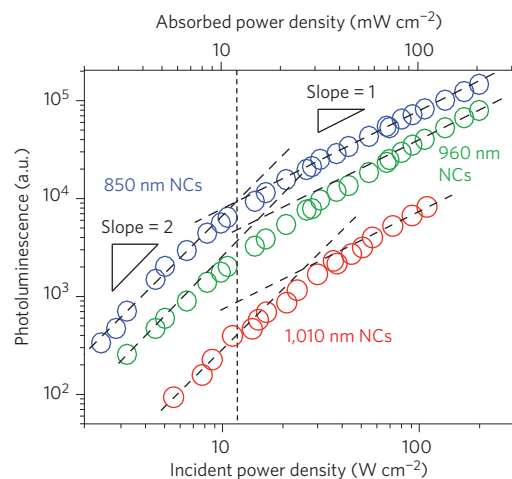


Figure 3 | Nanocrystal-sensitized upconverters reach peak efficiency at a sub-solar absorbed power density. Dependence of upconverted photoluminescence from 0.5% DBP in rubrene films on the incident light intensity when sensitized by $\lambda = 850$, 960, and 1,010 nm PbS NCs. The transition between quadratic and linear dependencies at 12 W cm^{-2} for the $\lambda = 850$ nm NCs indicates the minimum incident intensity for maximum-efficiency operation. With 0.1% absorption of the $\lambda = 808$ nm pump laser in the NC film, this corresponds to 12 mW cm^{-2} absorbed, which is less than the intensity of one sun.

$(143 \pm 41) \text{ mW cm}^{-2}$ respectively. We attain the highest quantum efficiencies when the NC layer is thin (\sim monolayer), probably due to a shorter diffusion path length to reach the bilayer interface as well as minimized re-absorption.

In TTA-based upconversion, an important parameter is the threshold excitation intensity at which the dependence of emission on incident light intensity transitions from quadratic to linear²⁴. Below the threshold, the triplet population varies linearly with excitation power because triplet decay is dominated by first-order loss processes. The upconverted emission via bimolecular TTA is therefore quadratic with pump intensity. However, when the triplet density is sufficiently high, TTA becomes the dominant decay

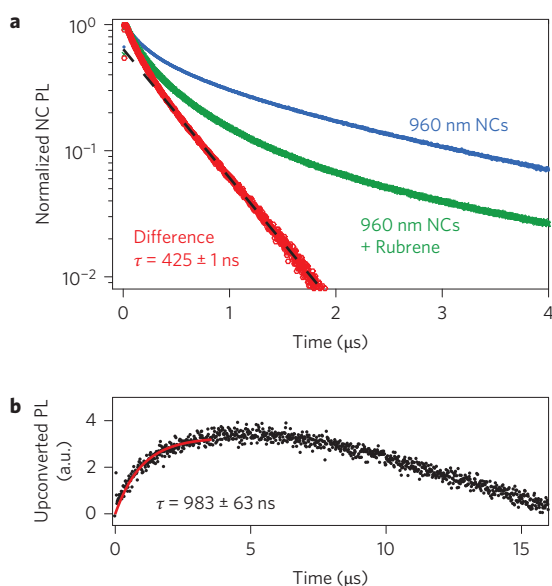


Figure 4 | Photoluminescence dynamics show slow, yet efficient triplet transfer. **a**, Quenching of the infrared emission from PbS NCs in the presence of rubrene doped with 0.5 vol% DBP. The extracted dynamics of active NCs (red) are largely mono-exponential with $\tau = 425 \pm 1$ ns (dashed black line). Accounting for competition with intrinsic decay channels ($\tau = 2.4 \pm 0.1$ μ s), we estimate the characteristic time of triplet transfer to be 520 ns. **b**, The corresponding rising dynamics of visible emission from the DBP are comprised of triplet transfer to rubrene, diffusion-mediated TTA, and energy transfer to the DBP, and show a characteristic mono-exponential time constant of 980 ns. The slow subsequent decay reflects the very long lifetime of isolated triplets in rubrene—so long that a fraction of photoexcitations survives until the subsequent excitation pulse 16 μ s later.

process, so the triplet density varies with the square root of the excitation flux. Thus, the intensity of upconverted emission becomes linear with pump power, and the efficiency saturates at its maximum value²⁴. Figure 3 shows that for the NC-sensitized thin-film samples, the transition occurs at 12, 17, and 26 W cm^{-2} for films with $\lambda = 850$, 960, and 1,010 nm NCs respectively. Maximum efficiencies are achieved at these incident light intensities even with the very low ($0.1 \pm 0.03\%$) absorption of the submonolayer NC film. We note that 12 mW cm^{-2} of absorbed pump light at $\lambda = 808$ nm generates 5×10^{16} excitons $\text{cm}^{-2} \text{s}^{-1}$, which is less than the available solar photon flux ($\lambda: 750\text{--}950$ nm, see Supplementary Information) and similar to the thresholds observed for efficient TTA in electrically pumped OLEDs²² (see Supplementary Information).

To reveal the underlying physical processes and identify further device optimization pathways, we measure the PL dynamics of our hybrid films. The dynamics of the neat film of $\lambda = 960$ nm NCs (Fig. 4a) are slow—multi-exponential at early times giving way to a mono-exponential decay with $\tau = 2.4 \pm 0.1$ μ s. This is consistent with the isolated-NC dynamics measured in solution (see Supplementary Information) plus some additional quenching, primarily at early times, probably via transfer to neighbouring NCs that are either permanently non-emissive or transiently dark due to blinking^{25,26}.

By contrast, the addition of the organic layer adds new decay pathways, clearly accelerating the PL decay at early times (<2 μ s). Subtraction of the emission from inactive NCs from the dynamics of the bilayer allows us to isolate the dynamics of active NCs (see Supplementary Information). We observe that the transfer dynamics are slow, with a dominant characteristic time of 520 ns. This is consistent with our previous work on the reverse

process—triplet transfer from organic materials to NCs—with these long oleic acid ligands¹⁹. Given the microsecond-scale intrinsic decay dynamics of PbS NCs, even these transfer rates kinetically outcompete other processes so that transfer is reasonably efficient ($>80\%$) from active NCs.

Lastly, to confirm that the quenching process is indeed energy transfer resulting in visible emission, we measure the rising dynamics of the PL from the DBP in the bilayer regions on the same film of $\lambda = 960$ nm NCs (Fig. 4b). We observe that all dynamics are slow, with the PL rising on a 980 ns timescale. This primarily reflects the additional time required for TTA to occur via diffusion (see Supplementary Information). The emission then decays much more slowly (>5 μ s), reflecting the very long lifetimes of isolated triplets in oligoacenes²⁷.

In conclusion, we demonstrate sensitization of TTA-based upconversion by PbS colloidal NCs, thereby reducing energy loss during sensitization, and enabling efficient solid-state upconversion from $\lambda > 1$ μ m to the visible. Given the bandgap tunability of NCs, this approach can be extended further into the infrared with molecular annihilators that have lower triplet energies than rubrene. Such upconversion, combined with broadband absorption and feasibility under low excitation power, offers a clear route towards surpassing the Shockley–Queisser limit in solar cells, and should enable new applications in sub-bandgap detector sensitization and three-dimensional displays.

Received 18 June 2015; accepted 13 October 2015;
published online 23 November 2015

References

- Singh-Rachford, T. N. & Castellano, F. N. Photon upconversion based on sensitized triplet–triplet annihilation. *Coord. Chem. Rev.* **254**, 2560–2573 (2010).
- Schmidt, T. W. & Castellano, F. N. Photochemical upconversion: the primacy of kinetics. *J. Phys. Chem. Lett.* **5**, 4062–4072 (2014).
- Schulze, T. F. & Schmidt, T. W. Photochemical upconversion: present status and prospects for its application to solar energy conversion. *Energy Environ. Sci.* **8**, 103–125 (2015).
- Zhou, J., Liu, Q., Feng, W., Sun, Y. & Li, F. Upconversion luminescent materials: advances and applications. *Chem. Rev.* **115**, 395–465 (2015).
- Trupke, T., Green, M. A. & Würfel, P. Improving solar cell efficiencies by upconversion of sub-band-gap light. *J. Appl. Phys.* **92**, 4117–4122 (2002).
- de Wild, J., Meijerink, A., Rath, J. K., van Sark, W. G. J. H. M. & Schropp, R. E. I. Upconverter solar cells: materials and applications. *Energy Environ. Sci.* **4**, 4835 (2011).
- Monguzzi, A. *et al.* Broadband up-conversion at subsolar irradiance: triplet-triplet annihilation boosted by fluorescent semiconductor nanocrystals. *Nano Lett.* **14**, 6644–6650 (2014).
- Cao, X., Hu, B. & Zhang, P. High upconversion efficiency from hetero triplet–triplet annihilation in multiacceptor systems. *J. Phys. Chem. Lett.* **4**, 2334–2338 (2013).
- Füchel, B. *et al.* Singlet oxygen mediated photochemical upconversion of NIR light. *J. Phys. Chem. Lett.* **2**, 966–971 (2011).
- Englman, R. & Jortner, J. The energy gap law for radiationless transitions in large molecules. *Mol. Phys.* **18**, 145–164 (1970).
- Singh-Rachford, T. N., Lott, J., Weder, C. & Castellano, F. N. Influence of temperature on low-power upconversion in rubbery polymer blends. *J. Am. Chem. Soc.* **131**, 12007–12014 (2009).
- Monguzzi, A., Tubino, R. & Meinardi, F. Multicomponent polymeric film for red to green low power sensitized up-conversion. *J. Phys. Chem. A* **113**, 1171–1174 (2009).
- Keivanidis, P. E., Balushev, S., Lieser, G. & Wegner, G. Inherent photon energy recycling effects in the up-converted delayed luminescence dynamics of poly(fluorene)-Pt^{II}octaethyl porphyrin blends. *ChemPhysChem* **10**, 2316–2326 (2009).
- Mahato, P., Monguzzi, A., Yanai, N., Yamada, T. & Kimizuka, N. Fast and long-range triplet exciton diffusion in metal–organic frameworks for photon upconversion at ultralow excitation power. *Nature Mater.* **14**, 924–930 (2015).
- Moreels, I. *et al.* Size-dependent optical properties of colloidal PbS quantum dots. *ACS Nano* **3**, 3023–3030 (2009).
- Weidman, M. C., Beck, M. E., Hoffman, R. S., Prins, F. & Tisdale, W. A. Monodisperse, air-stable PbS nanocrystals via precursor stoichiometry control. *ACS Nano* **8**, 6363–6371 (2014).

17. Efros, A. L. *et al.* Band-edge exciton in quantum dots of semiconductors with a degenerate valence band: Dark and bright exciton states. *Phys. Rev. B* **54**, 4843–4856 (1996).
18. Huang, Z. *et al.* Hybrid molecule–nanocrystal photon upconversion across the visible and near-infrared. *Nano Lett.* **15**, 5552–5557 (2015).
19. Thompson, N. J. *et al.* Energy harvesting of non-emissive triplet excitons in tetracene by emissive PbS nanocrystals. *Nature Mater.* **13**, 1039–1043 (2014).
20. Tabachnyk, M. *et al.* Resonant energy transfer of triplet excitons from pentacene to PbSe nanocrystals. *Nature Mater.* **13**, 1033–1038 (2014).
21. Debad, J. D., Morris, J. C., Lynch, V., Magnus, P. & Bard, A. J. Dibenzotetraphenylperiflanthene: synthesis, photophysical properties, and electrogenerated chemiluminescence. *J. Am. Chem. Soc.* **118**, 2374–2379 (1996).
22. Kondakov, D. Y., Pawlik, T. D., Hatwar, T. K. & Spindler, J. P. Triplet annihilation exceeding spin statistical limit in highly efficient fluorescent organic light-emitting diodes. *J. Appl. Phys.* **106**, 124510 (2009).
23. de Mello, J. C., Wittmann, H. F. & Friend, R. H. an improved experimental determination of external photoluminescence quantum efficiency. *Adv. Mater.* **9**, 230 (1997).
24. Haefele, A., Blumhoff, J., Khayzr, R. S. & Castellano, F. N. Getting to the (square) root of the problem: how to make noncoherent pumped upconversion linear. *J. Phys. Chem. Lett.* **3**, 299–303 (2012).
25. Cui, J., Beyler, A. P., Bischof, T. S., Wilson, M. W. B. & Bawendi, M. G. Deconstructing the photon stream from single nanocrystals: From binning to correlation. *Chem. Soc. Rev.* **43**, 1287–1310 (2013).
26. Whitcomb, K. J., Ryan, D. P., Gelfand, M. P. & Van Orden, A. Blinking statistics of small clusters of semiconductor nanocrystals. *J. Phys. Chem. C* **117**, 25761–25768 (2013).
27. Reineke, S. & Baldo, M. A. Room temperature triplet state spectroscopy of organic semiconductors. *Sci. Rep.* **4**, 3797 (2014).

Acknowledgements

This work was supported as part of the Center for Excitronics, an Energy Frontier Research Center funded by the US Department of Energy, Office of Science, Office of Basic Energy Sciences under Award Number DE-SC0001088 (MIT). The authors thank P. Deotare for assistance with optical measurements, as well as J. M. Scherer, C-H. Chuang, P. R. Brown and M. Sponceller for assistance with nanocrystal synthesis.

Author contributions

M.Wu and D.N.C. fabricated the samples. M.Wu measured absorption spectra and the intensity dependence. D.N.C. measured excitation spectra and the yield of upconversion. M.W.B.W. made the transient PL measurements and synthesized the nanocrystals. M.Wu and J.J. prepared nanocrystal solutions for sample fabrication and performed AFM measurements. N.G. and M.Welborn simulated the nanocrystal structure. The project was conceived by M.A.B. All authors discussed the results and commented on the manuscript.

Additional information

Supplementary information is available in the [online version](#) of the paper. Reprints and permissions information is available online at www.nature.com/reprints. Correspondence and requests for materials should be addressed to V.B., M.G.B. and M.A.B.

Competing financial interests

MIT has filed an application for patent based on this technology that names D.N.C., M.Wu, M.W.B.W., V.B., M.G.B., and M.A.B. as inventors.

Solid-state infrared-to-visible upconversion sensitized by colloidal nanocrystals

Mengfei Wu[†], Daniel N. Congreve[†], Mark W.B. Wilson[†],
Joel Jean, Nadav Geva, Matthew Welborn, Troy Van Voorhis,
Vladimir Bulović*, Mounqi G. Bawendi*, and Marc A. Baldo*

*Correspondence to: bulovic@mit.edu, mgb@mit.edu, baldo@mit.edu

[†] contributed equally

Supplementary Information

PbS nanocrystal synthesis

The lead sulphide (PbS) colloidal nanocrystals (NCs) capped with oleic acid were synthesized following literature methods^{1,2}. Lead(II) acetate trihydrate (PbAc), bis(trimethylsilyl)sulphide ((TMS)₂S), oleic acid (OA), 1-octadecene (ODE), methanol, butanol, hexane, and octane (all solvents anhydrous) were purchased from Sigma-Aldrich and used as received. 11.38 g PbAc was dissolved in a mixture of OA and ODE (300 mL total) and degassed at 100°C overnight. This solution was heated to the desired injection temperature (90–150°C), and a solution of 3.15 mL (TMS)₂S and 150 mL ODE was rapidly injected. The NC size was controlled by varying the ODE:OA ratio, the injection temperature, and the time before removal of the heating mantle immediately after injection. As-synthesized NCs were precipitated with butanol, methanol, and/or acetone, re-dispersed in hexane, and stored as a stock solution at high concentration. Prior to sample fabrication, NCs were purified twice more with butanol and acetone, then re-dispersed in octane. All synthesis and purification steps were performed in nitrogen atmosphere.

Sample fabrication

Glass substrates were cleaned by sequential sonication in Micro-90 detergent solution, deionized water, and acetone. They were then immersed in boiling isopropanol and dried under a stream of pure nitrogen. The substrates were then transferred to a nitrogen glovebox. For each of the three sizes, the PbS NCs were dissolved in octane at a concentration of 1 mg/mL, and spin-cast onto the cleaned glass at 2500 rpm for 60 seconds, with a ramp rate of 2000 rpm/s.

Without exposing the sample to air, an 80 nm-thick layer of rubrene, or rubrene doped with dibenzotetraphenylperiflanthene (DBP) was then thermally evaporated at pressures less than 3×10^{-6} Torr in a thermal evaporator (Angstrom Engineering) directly attached to the glovebox. The DBP was purchased from Sigma-Aldrich and used as received. The rubrene was purchased from Luminescent Technologies Inc. and used as received. Samples were encapsulated in the glovebox using two-part epoxy (Devcon 5 Minute®) and a second glass substrate.

Sample morphology

The AFM image (Fig. S1a) of a thin layer of NCs prepared as described above shows sub-monolayer coverage. The scans reveal mixed regions of glass and NCs. The areas covered with NCs are mostly monolayer (~5 nm), although multi-layer islands also form at some sites.

To improve adhesion of NCs to the glass substrate, we soaked the substrates overnight in a solution of 12 mM (3-mercaptopropyl)trimethoxysilane (3-MPTMS) in toluene, then sonicated them for 1 minute in 2-propanol to remove unbound 3-MPTMS. Figure S1b shows improved coverage of NCs. We characterized samples fabricated on both untreated and treated glass substrates, and found that the two had similar performance although those treated typically degraded more rapidly. Results presented in the main text were all from samples on untreated substrates.

Steady-state optical measurements

Emission spectra

The samples were excited with a $\lambda = 808$ nm continuous-wave (CW) laser at an angle of incidence of ~ 35 degrees. The photoluminescence (PL) normal to the sample was captured by a collimating lens and subsequently focused down onto a fiber port coupled to an Ocean Optics USB2000 spectrometer. A dielectric short-pass filter (Thorlabs FESH0750) was used to eliminate stray pump light.

Upconversion quantum efficiency

As described in the main text, we follow literature convention (particularly the definition on page 401 of the comprehensive review from Zhou *et al.*³) and define the upconversion quantum efficiency (our η , Zhou *et al.*'s QE_{UC}) as “the fraction of absorbed photons that serve to generate upconversion emission.” In addition to allowing for the straightforward comparison of our work to the majority of the literature on TTA-based upconversion, this definition has the intuitive advantage that perfect (two-to-one) upconversion corresponds to a device with 100% efficiency.

We measured the photoluminescence quantum yield (PLQY) of the bilayer samples at two excitation wavelengths: $\lambda = 808$ nm, which led to upconverted emission, and $\lambda = 460$ nm, where emission came from direct photoexcitation of the organic material. Comparison between the two PLQYs reveals the intrinsic efficiency pertaining to the upconversion process, namely energy transfer and TTA. Thus, in terms of the experimental observables, we obtain the upconversion quantum efficiency from:

$$\eta = \frac{PLQY_{UC}}{PLQY_{organic}}$$

where $PLQY_{organic}$ was measured with excitation at $\lambda = 460$ nm, calculated as the ratio of emitted photons to absorbed photons, and $PLQY_{UC}$ was measured at $\lambda = 808$ nm, having a factor of two multiplied to that ratio, specifically for upconversion for reasons outlined above.

As discussed by Zhou *et al.*³, a relative measurement with respect to a fluorescence standard is commonly employed for solution-based systems. However, this is not suitable for solid-state thin films as those generally have anisotropic emission. Instead, we measured the

PLQY of our solid-state devices in an integrating sphere (Labsphere RTC-060-SF) following the technique from de Mello *et al.*⁴ In this technique, three measurement configurations are involved: A) sample out of the sphere, B) sample in the sphere but off the incident beam path, and C) sample in the sphere and in the incident beam path. The first-pass absorption (*Abs*) is obtained from:

$$Abs = 1 - \frac{L_C}{L_B}$$

where *L* is the number of laser photons exiting the sphere, and the subscript denotes the measurement configuration. PLQY is obtained from:

$$PLQY = \frac{P_C - (1 - Abs)P_B}{L_A \cdot Abs}$$

where *P* is the number of emitted photons collected from the sphere.

In practice, when pumping at $\lambda = 808$ nm, for configuration C, we positioned the sample so that the laser beam (91 mW) fell upon the edge of the glass substrate, and was efficiently coupled to modes of the slab waveguide. We adopted this total-internal-reflection-fluorescence (TIRF)-like geometry to boost sample absorption to 5-10% (see Table S1). The conventional near-normal incidence had posed difficulty in measuring the sub-monolayer NC absorption accurately given the noise floor of the sphere. For configuration B, there was negligible upconverted emission (below our detection limit). Light was captured at the exit port of the sphere and focused onto an Ocean Optics USB2000 spectrometer. The laser power was determined by collecting the unfiltered laser light from the sphere at 30 ms integration time averaged over many integration periods. The intensity of the upconverted emission was determined by collecting the light from the output of the sphere through a dielectric short-pass filter (Thorlabs FESH0750) with an integration time of 60 s. The respective measurements were normalized to the same integration time.

The PLQY of the emissive organic material alone ($PLQY_{\text{organic}}$) was determined in the same sphere by exciting the same sample with a $\lambda = 460$ nm CW laser. The laser power was determined with a 200 ms integration time without any filters. The emission was measured through a long-pass filter (Thorlabs FELH0500) with a 4 s integration time. Here, the emission resulting from diffuse excitation in configuration B (P_B) was not negligible. We also note that the absorption of the sample at 460 nm is dominated by the organic film, rather than the sub-monolayer of NCs.

In all of the above measurements, the wavelength-dependent response of the sphere, the spectrometer, as well as the dielectric filters used were calibrated to a silicon photodetector with known responsivity. We also verified that the intensity of the signal as measured by the spectrometer scaled linearly with integration time.

The measured values obtained by this method are given in Table S1 below. We note that since the annihilator is kept constant for the varying NC sizes, the decrease in η for smaller-gap NCs indicates that the number of excitations transferring decreases. This could result from less efficient net energy transfer or an increase in non-radiative pathways in the NCs at lower energies⁵. In the *Transient measurements* section, below, we present further data on the energy transfer efficiency and the lifetime of the different-sized NCs.

Table S1. Measurement of upconversion quantum efficiency

NC size $\lambda_{\text{first-exciton}}$	Absorption $\lambda_{\text{ex}} = 808 \text{ nm}$	$PLQY_{\text{UC}}$ $\lambda_{\text{ex}} = 808 \text{ nm}$	$PLQY_{\text{organic}}$ $\lambda_{\text{ex}} = 460 \text{ nm}$	Upconversion QE η
850 nm	5.7±0.2%	0.57±0.05%	46.3±4.2%	1.23±0.16%
960 nm	7.8±0.3%	0.23±0.02%	44.7±4.1%	0.51±0.07%
1010 nm	11.0±0.5%	0.10±0.01%	46.9±4.3%	0.21±0.03%

Edge-coupling rendered it difficult to measure the excitation intensity directly. However, we could instead calculate the absorbed intensities based on the absorbed pump power and geometry. With 91 mW of $\lambda = 808 \text{ nm}$ light incident on the edge of the glass substrate, we observed a visible stripe, $0.35 \pm 0.10 \text{ mm}$ thick, across 20 mm of the sample. Thus, from the measured fractional absorption for each sample (Table S1), the absorbed optical intensities were 74 ± 21 , 101 ± 29 and $143 \pm 41 \text{ mW cm}^{-2}$, respectively (see Table S2). These values are at least five times greater than the separately-measured absorbed intensities required to reach the linear threshold (*i.e.* 12, 17 and 26 mW cm^{-2}) for the three different-sized NCs, respectively (see Fig. 3 in the main text). Thus, the efficiencies in Table S1 were measured in the linear regime, and are therefore the maximum achievable for each particular device.

Table S2. Calculation of absorbed intensities for efficiency measurement

NC size	Power	Absorption	Excitation area	Absorbed intensity (mW cm ⁻²)	Uncertainty (mW cm ⁻²)
850 nm	91 mW	5.7±0.2%	0.35±0.10 mm	74	±21 (28.8%)
960 nm		7.8±0.3%	×	101	±29 (28.8%)
1010 nm		11.0±0.5%	20 mm	143	±41 (28.9%)

Effect of doping rubrene with DBP

We prepared two samples both sensitized by the $\lambda = 850$ nm NCs, one with rubrene doped with 0.5 vol% DBP as the annihilator, and the other with neat rubrene. The measurement setup was the same as described in the section *Emission spectra*. We first excited the samples at $\lambda = 808$ nm, and observed that the intensity of the upconverted emission from the doped rubrene sample was 19 times higher than the neat rubrene sample at their respective peak wavelengths ($\lambda_{\text{Rb}} = 573$ nm, $\lambda_{\text{DBP}} = 612$ nm). See Fig. S2a. We then directly excited the annihilators with the $\lambda = 460$ nm laser. The PL intensity from doped rubrene was 16 times higher. See Fig. S2b. This indicates that the enhancement in the upconverted emission is largely due to an increase in the fluorescence quantum yield of the organic film when rubrene is doped with DBP. Mechanistically, we consider that this results from the exothermic Förster resonant energy transfer of singlet excitons from poorly-emissive rubrene to the highly-emissive dye. Given that primary decay channel for a singlet exciton (however generated) in neat rubrene is fission to a triplet pair^{6,7}, the good absolute PLQY of the doped film (46±4%) suggests that energy transfer to DBP kinetically out-competes the ~110 ps fission process⁸.

Intensity dependence

The measurement setup was the same as described in the section *Emission spectra*. The incident power at $\lambda = 808$ nm was varied with neutral density filters across about two orders of magnitude. We collected the upconverted emission with the spectrometer and integrated the area under the spectra. The incident power was determined with a calibrated power meter (Thorlabs S130C and PM100A). To determine the spot size of the laser beam, we measured the incident

power through a pinhole with a photodiode mounted on a micro-positioning stage while we scanned in the x and y directions. The spot size was $263 \times 215 \mu\text{m}$ (FWHM). Power densities were then calculated based on the total incident power and the spot size.

Absorption

To determine the equivalent absorbed power for the intensity dependence, absorption of the sub-monolayer NC films at $\lambda = 808 \text{ nm}$ was measured indirectly using a scaling method. We prepared two samples for each NC size: a sample spun from 1 mg mL^{-1} solution at 2500 rpm, yielding the same thickness as in upconverting samples, and a thicker film spun from 10 mg mL^{-1} solution at 1500 rpm. These samples consisted of the NCs only without the organics and were encapsulated. We also prepared a control with a piece of clean glass encapsulated with another piece of glass. Absorption spectra, see Fig. S3, were measured with an Agilent Cary 5000 UV-vis-NIR spectrophotometer, at normal incidence, and obtained from the difference between the transmission of the double-glass control and the sample transmission. Each spectrum in Fig. S3 is an average of 2 to 4 scans. We note that the optical density (O.D.) of the sub-monolayer films at $\lambda = 808 \text{ nm}$ cannot be resolved from the measurement uncertainty. However, their O.D. at shorter wavelengths, *e.g.* $\lambda = 400 \text{ nm}$, has a larger signal-to-noise ratio. The thick film has measurable O.D. at both $\lambda = 400 \text{ nm}$ and $\lambda = 808 \text{ nm}$. See also Table S3. Assuming O.D. scales linearly with effective thickness at all wavelengths, we compute the O.D. at $\lambda = 808 \text{ nm}$ for the sub-monolayer according to:

$$O.D._{(\text{thin},808 \text{ nm})} = \frac{O.D._{(\text{thin},400 \text{ nm})}}{O.D._{(\text{thick},400 \text{ nm})}} O.D._{(\text{thick},808 \text{ nm})}$$

From O.D. values, we calculate the % absorption:

$$\%Abs = (1 - 10^{-O.D.}) \times 100\%$$

The results are listed in Table S3. These are then multiplied by a geometric factor of $1/\cos 35^\circ = 1.22$ to account for the oblique angle of incidence in the measurement setup used for the intensity-dependent measurements. The top axis in Fig. 3 in the main text used 0.1% absorption, corresponding to that of $\lambda = 850 \text{ nm}$ NCs.

Excitation spectrum

The excitation spectrum was measured utilizing a SuperK Extreme (K94-120-12) supercontinuum laser (NKT Photonics) coupled into a monochromator (Princeton Instruments SpectraPro 2150). The intensity was adjusted such that it was constant at every excitation wavelength used in the measurement. The integrated emission from the organic was collected with a silicon photodiode through appropriate filters and coupled to a lock-in amplifier, as the excitation wavelength was scanned.

Nanocrystal and rubrene simulations

Molecular dynamics calculations were performed to determine the structure of ligands on the surface of the NC. An NVT simulation was run at 300K for 2 ns with a time step of 2 ps using the Velocity Verlet integrator. Temperature was controlled using the Anderson thermostat with a coupling time of 100 fs. The force field was OPLS⁹ for the oleic acid, and a Lennard-Jones-Coulombic potential for the NC (following the methodology used in Schapotschnikow *et al.*¹⁰) The NC is PbS in the rocksalt crystal structure carved from a bulk crystal with a Wulff parameter of ~ 0.8 between the $\{100\}$ and the $\{111\}$ planes. It is about 4.9 nm in diameter and contains 2000 atoms. The NC is decorated with 150 oleic acid ligands.

Electronic structure calculations were performed on a four-rubrene cell using the Local Spin Density Approximation functional with a STO-3G basis set. Structures were taken from crystalline rubrene. The paired triplet state was computed as the lowest quintet state of the four-molecule system. The singlet state was computed using the Δ SCF¹¹ method. The isosurfaces shown are density differences between the ground state and the state of interest.

Transient measurements

Apparatus

We used time-correlated single-photon counting to measure the PL dynamics of the upconversion process. Samples were excited at $\lambda = 785$ nm by the emission of a pulsed laser (PicoQuant LDH-P-C-780) passed through a band-pass cleanup filter (ThorLabs FBH780-10). This wavelength is well below the optical gaps of rubrene or DBP, so that the pump pulse is selectively absorbed by the NCs.

To measure the decay dynamics of the short-wave infrared (SWIR) PL from the NCs, the samples were excited by a 100 kHz train of ~ 100 ps pulses that were attenuated to yield pulse irradiances from 1-10 pJ/cm². This low repetition rate allowed the emission from the long-lived excitations in the NCs to decay below 10^{-2} of the peak intensity, to minimize the build-in of a quasi-steady-state excitation density. Since the quenching dynamics were effectively independent of excitation intensity (Fig. S4), the pump power was scaled to achieve a $\sim 5\%$ stop rate in each measurement. The emission from the NCs was collected and imaged using reflective optics onto an InGaAs/InP single-photon counting avalanche photodiode (Micro Photon Devices SIR-DH-025-C), fitted with a long-pass filter (Chroma Technology Corp. ET900LP) to remove scattered photons from the excitation laser. Decay histograms were generated by recording photon arrivals using a PicoQuant PicoHarp.

Decomposition

We used a shadow mask during organic deposition so that it was possible to optically access both bilayer regions and areas with the sub-monolayer NC film alone on each sample. When comparing the measured dynamics of the two regions on several samples, it was apparent that the dynamics from all bilayers evolve to match those measured for their respective NC-only regions after ~ 3 μ s. As a result, we assert a simple model where there are two sub-populations of NCs: those which are able to transfer excitations to the organic (active), and those which are not (inactive). In addition to kinetic competition, this could arise from morphological heterogeneity which may leave some NCs distant from a hetero-interface, which is consistent with our AFM data (Fig. S1).

Under this model, the fraction of inactive NCs is given by the ratio of the late-time decay amplitudes when the data is normalized to the peak. We observe that this fraction varies among films (Fig. S5), and that 63% of the NCs are active for the sample in Fig. 4 in the main text. The presence of inactive NCs highlights that as the NC film is thickened in the future to improve absorption, it will be critical to ensure efficient harvesting of excitons generated further away from the bilayer interface, which may be achieved through exciton funneling in cascaded NC structures¹².

Accordingly, we isolate the dynamics of active nanocrystals by subtracting a scaled copy of the nanocrystal-only decay from the bilayer dynamics. The resulting dynamics are largely mono-exponential, but include some more-rapid decay components at earlier times. These could stem from sub-populations of active NCs with accelerated transfer rates (due to local geometry), imperfect removal of the contribution from inactive NCs, or the natural limitations of our simple two-population model.

To estimate the characteristic time of transfer, τ_{trans} , we fit a mono-exponential function to the long-time ($t > 500$ ns) region of the extracted transfer dynamics, where the decay is obviously linear on a semi-log plot. We consider that this total decay results from simple kinetic competition between transfer and intrinsic decay processes, so we calculate the characteristic time of transfer by:

$$\tau_{\text{trans}} = \left(\frac{1}{\tau_{\text{tot}}} - \frac{1}{\tau_{\text{intrinsic}}} \right)^{-1}$$

Figures S5a & b show example decompositions of the decay dynamics from bilayer films with $\lambda = 850$ nm and $\lambda = 1010$ nm NCs, respectively. We note that the decay dynamics of the $\lambda = 1010$ nm dots were typically affected much less strongly by the presence of rubrene than those of other NCs. This implies that the quenching via energy transfer in these samples is weaker, which is consistent with the comparatively poor upconversion efficiencies found in the steady-state measurements.

Solution Measurements

This transient SWIR PL apparatus was also used to measure the decay dynamics of the NCs used in these devices dispersed in a dilute hexane solution under a nitrogen atmosphere. As shown in Fig. S6, the decay dynamics of isolated NCs are mono-exponential, with $\tau = 3.4 \mu\text{s}$ for $\lambda = 850 \text{ nm}$, $\tau = 3.3 \mu\text{s}$ for $\lambda = 960 \text{ nm}$, and $\tau = 2.5 \mu\text{s}$ for the $\lambda = 1010 \text{ nm}$ NCs. The more rapid decay of the emission from longer-wavelength NCs is consistent with a reduced PLQY⁵.

Visible Measurements

The same basic apparatus was used to measure the rising dynamics of the visible emission from the DBP following triplet transfer to rubrene, TTA, and FRET, with the following changes: The detector was replaced with a silicon SPAD (Micro Photon Devices SPD-100-C0C), the pump scatter was suppressed with short-pass filter (ThorLabs FESH0700), and the diode was overdriven to increase the pulse energy, so that the pulse duration was $\sim 1 \text{ ns}$.

As shown in Fig. S7b and discussed in the main text, the decay timescale of excitations in the rubrene is very long ($>5 \mu\text{s}$), so the dynamics we observe arise in the presence of a substantial quasi-steady-state population. Although this long excited-state lifetime enables efficient upconversion at low excitation rates, an associated consequence is that excitations in the organic, likely trapped triplet excitons¹³, survive until the next excitation pulse, building up a quasi-steady-state population of triplets. This is consistent with our observation that the time-integrated PL intensity varies with the square of the repetition rate in this regime.

In order to verify this, we measured the dynamics of the visible rise while varying the repetition rate of the excitation pulse. As expected, the greatest modulation of the signal by the absorption of the pump pulse occurs at the lowest achievable excitation rate—this was 60 kHz due to limitations of our timing hardware and the signal-to-noise ratio. As shown in Figs. S7a & b, the dynamics of the rise of the visible signal accelerate at higher repetition rates—as diffusion-mediated TTA is faster at higher triplet densities in the organic—to approach the transfer rate extracted from the quenching measurements.

Calculations on sub-solar threshold intensity

Figure S8a shows the normalized absorption spectra of films made from three sizes of PbS NCs, as well as rubrene doped with 0.5 vol% DBP. Figure S8b shows the AM1.5(Global) solar spectrum plotted in units of spectral irradiance. Figure S8c presents the same spectrum plotted in units of spectral photon flux (*i.e.* photons per unit time per unit area per nm of spectrum), which is obtained by dividing the irradiance data by hc/λ for each spectral bin. Thus, we can determine either the available intensity or solar photon flux by integrating over a selected spectral range on the relevant data set.

To estimate the photon flux available to each of our upconverter devices under solar illumination, we define the relevant spectral window, and integrate the area under the curve in Fig. S8c. For all devices, we consider the photon flux beyond $\lambda = 750$ nm, where the organic absorption falls below our detection limit (see Figure S8a). For the $\lambda = 850$ nm NCs, we integrate out to $\lambda = 950$ nm—a conservative estimate of the absorption edge—giving a total flux of 7.34×10^{16} photons $\text{cm}^{-2} \text{s}^{-1}$. Similarly, we calculate the solar photon flux that can be utilized for upconversion sensitized by $\lambda = 960$ nm NCs to be 1.06×10^{17} photons $\text{cm}^{-2} \text{s}^{-1}$ (λ : 750–1050 nm), and that by $\lambda = 1010$ nm NCs to be 1.22×10^{17} photons $\text{cm}^{-2} \text{s}^{-1}$ (λ : 750–1100 nm).

As stated in the main text, for monochromatic excitation at $\lambda = 808$ nm, the threshold absorbed intensities for linear-regime operation are 12, 17, and 26 mW cm^{-2} for the three sizes of NCs. In units of flux, these thresholds are 4.9×10^{16} , 6.9×10^{16} , and 1.1×10^{17} photons $\text{cm}^{-2} \text{s}^{-1}$, respectively—all lower than the available solar photon fluxes. Therefore, we conclude that if all photons in the relevant wavelength range could be captured by the NCs and lead to similar exciton dynamics, sufficient triplet excitons would be generated from sub-solar excitation to reach the linear regime, *i.e.* achieving the maximum upconversion efficiency.

We also compare the threshold triplet exciton density in our devices with that in organic light-emitting diodes employing the same rubrene-DBP annihilator-emitter thin film (Kondakov *et al.*¹⁴). There, the authors observe “a clear switchover between quadratic and linear regimes in the 1–3 mA/cm^2 range”. This current density corresponds to an areal generation of $0.6\text{--}1.9 \times 10^{16}$ excitons $\text{cm}^{-2} \text{s}^{-1}$, which is slightly lower than the threshold we observe. However, noting that a fraction of excited NCs are inactive in our present devices (see above), and that Kondakov *et al.* used a thinner organic layer (30 nm vs. our 80 nm), the threshold triplet densities are similar.

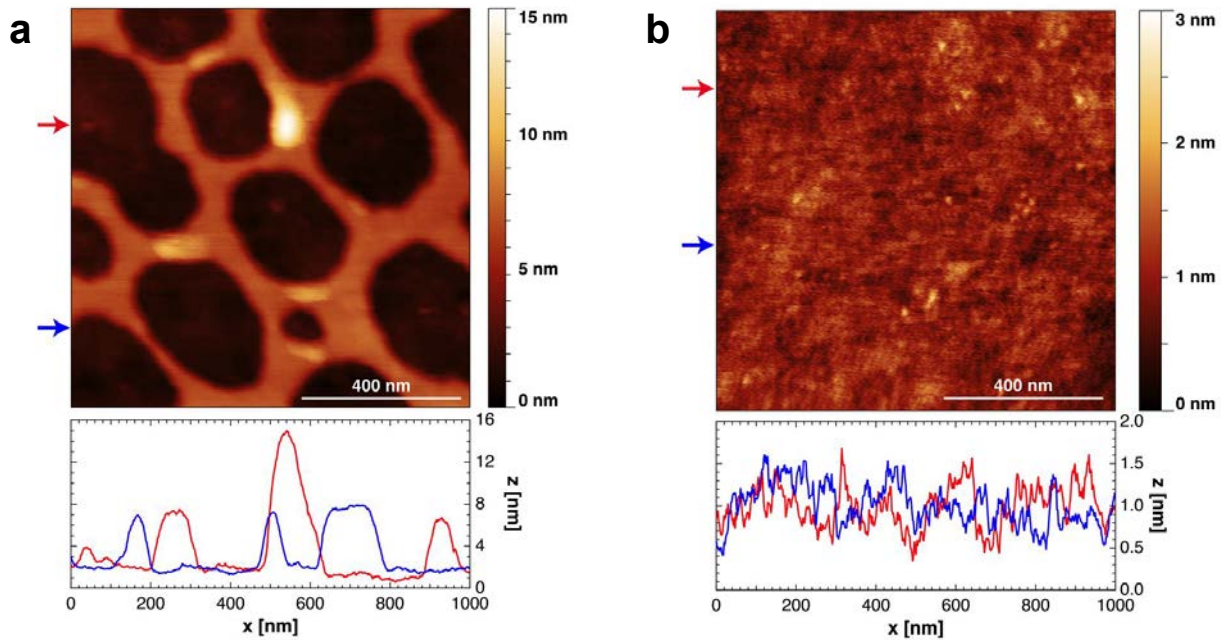


Figure S1. AFM image of the $\lambda = 1010$ nm nanocrystals, spin-cast from 1 mg mL^{-1} solution at 2500 rpm (a) on untreated glass substrate, showing sub-monolayer coverage with higher islands, and (b) on 3-MPTMS treated glass substrate, demonstrating more uniform coverage.

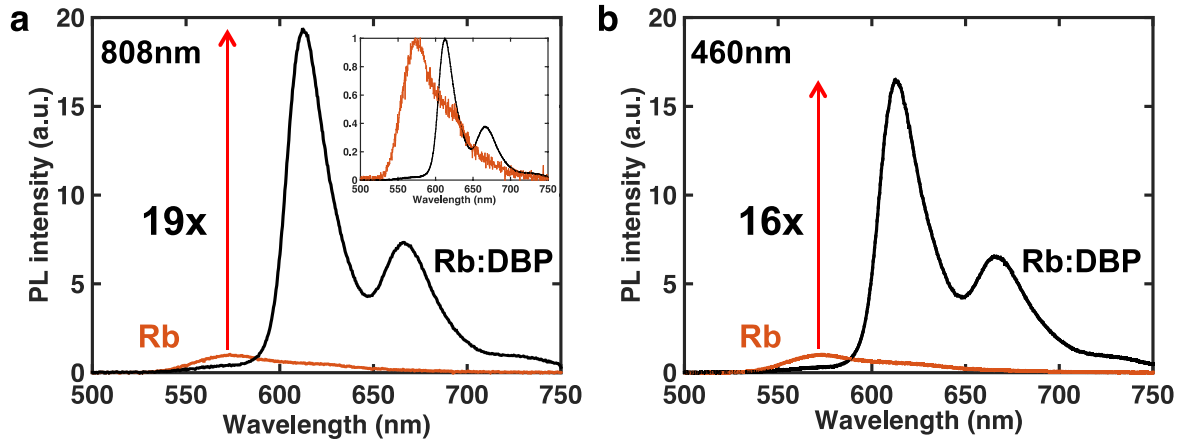


Figure S2. Comparison of the PL intensity with the two annihilators: rubrene (Rb, brown) and rubrene:DBP (black), both with the $\lambda = 850$ nm nanocrystals as the sensitizer. Laser excitation is at (a) $\lambda = 808$ nm and (b) $\lambda = 460$ nm. The shapes of the normalized emission spectra are compared in the inset of (a).

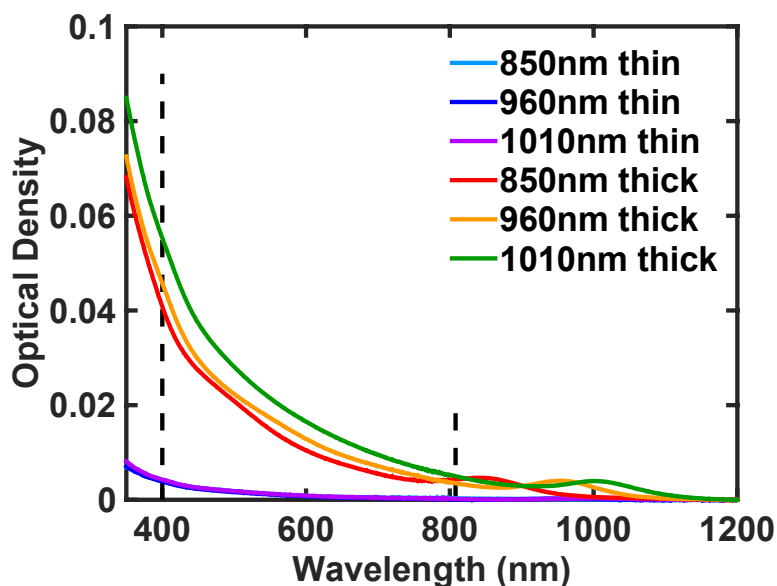


Figure S3. Absorption spectra of the encapsulated thin films of PbS nanocrystals (NCs). The legend indicates the first excitonic absorption peak of the NCs and the thickness of the film. Thin samples were spun from 1 mg mL^{-1} at 2500 rpm, while thick ones were spun from 10 mg mL^{-1} at 1500 rpm. The dashed lines at $\lambda = 400 \text{ nm}$ and $\lambda = 808 \text{ nm}$ highlight the values used to determine the sub-monolayer absorption.

Table S3. Calculation of sub-monolayer absorption

NC size	Optical Density				% Absorption
	Thick, 400 nm (measured)	Thin, 400 nm (measured)	Thick, 808 nm (measured)	Thin, 808 nm (calculated)	Thin, 808 nm (calculated*)
850 nm	0.0410 ± 0.0004	0.0035 ± 0.0007	0.0043 ± 0.0005	0.00037 ± 0.00012	0.08 ± 0.03
960 nm	0.0459 ± 0.0002	0.0038 ± 0.0009	0.0035 ± 0.0004	0.00029 ± 0.00010	0.07 ± 0.03
1010 nm	0.0555 ± 0.0004	0.0043 ± 0.0004	0.0050 ± 0.0003	0.00039 ± 0.00006	0.09 ± 0.02

* at normal incidence. A geometric factor of 1.22 is multiplied to the numbers to account for the angle of incidence at 35° .

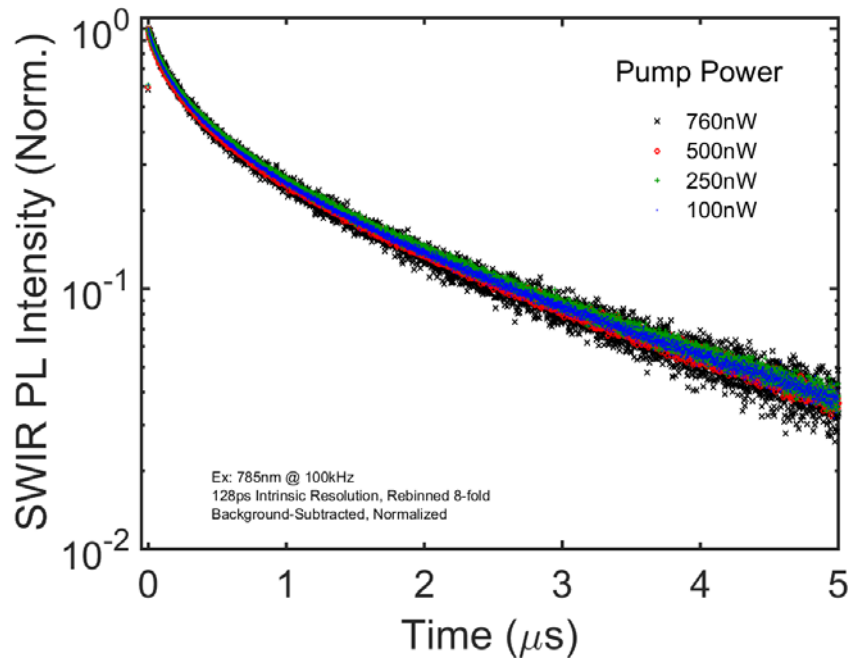


Figure S4. The decay dynamics of the infrared emission from a typical bilayer film (DBP-doped rubrene and a film of PbS nanocrystals with a first exciton absorption of $\lambda = 850$ nm) are independent of excitation intensity in the measurement regime.

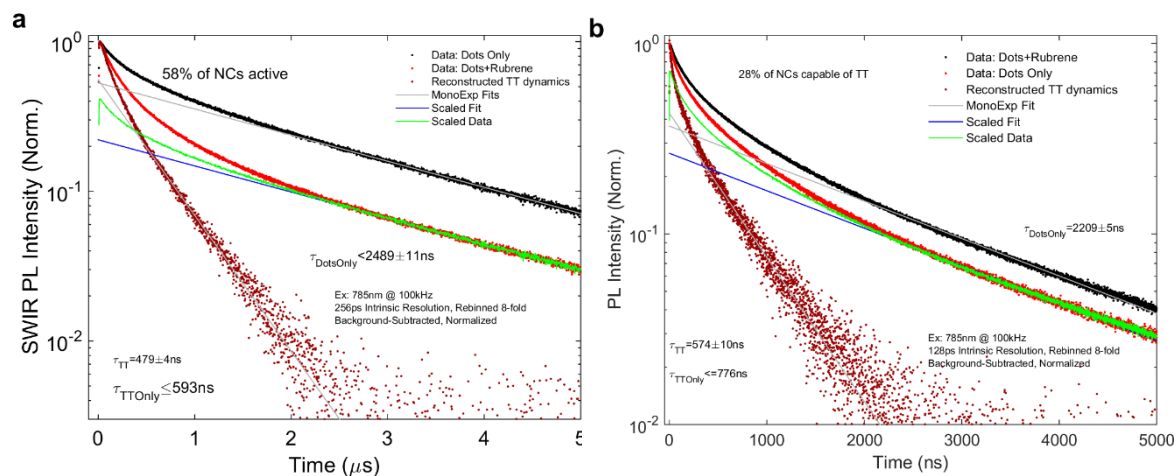


Figure S5. PL decay dynamics of bilayer films with (a) $\lambda = 850 \text{ nm}$ and (b) $\lambda = 1010 \text{ nm}$ nanocrystals. The same decomposition procedure (described above) used to generate Fig. 4 in the main text was employed to extract the quenching dynamics due to triplet transfer to the rubrene film.

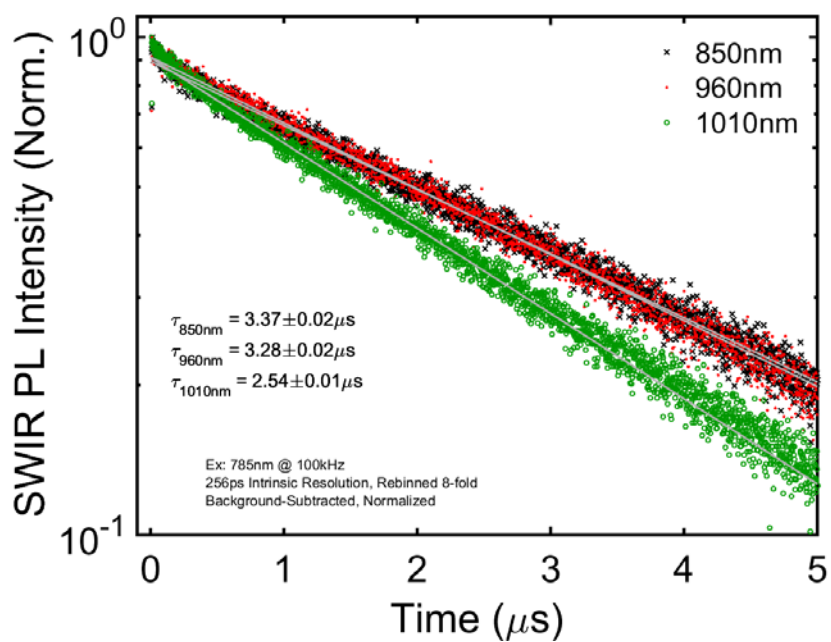


Figure S6. Decay dynamics of the nanocrystals used in this work measured in dilute hexane solution.

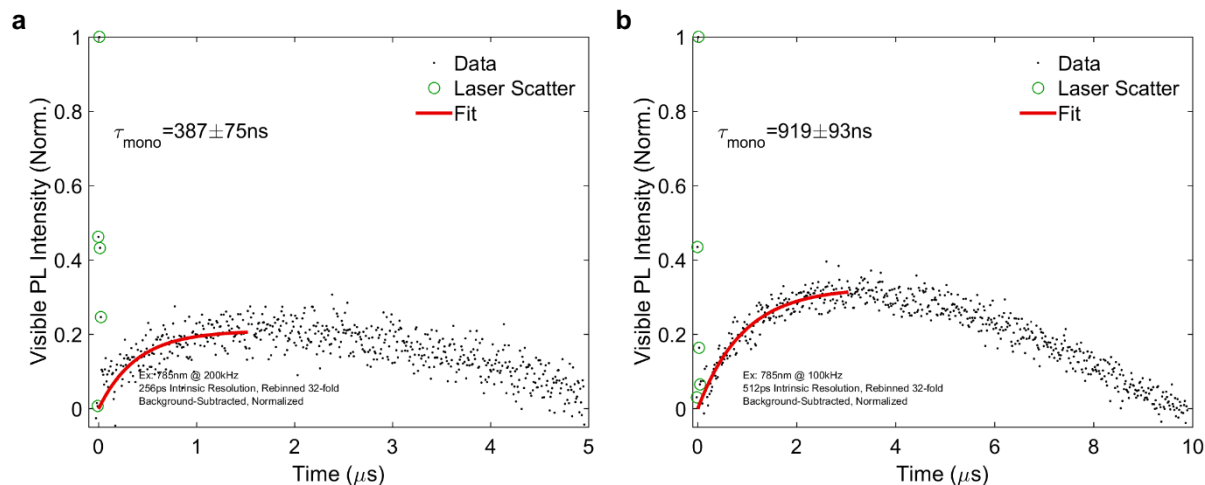


Figure S7. Dynamics of the visible DBP emission following selective excitation of the PbS nanocrystals (NCs) and upconversion. These data were taken on the same sample ($\lambda = 960 \text{ nm}$ NCs) as used for Fig. 4b in the main text. Here, the excitation is at a faster repetition rate of (a) 200 kHz and (b) 100 kHz. The data (excepting points obviously contaminated with laser scatter) is fit to a mono-exponential rise to gauge the combined timescale of triplet transfer, TTA, FRET to the DBP, and emission. The accelerated dynamics reflect the more rapid timescale of diffusion-mediated TTA with higher effective exciton densities in the rubrene.

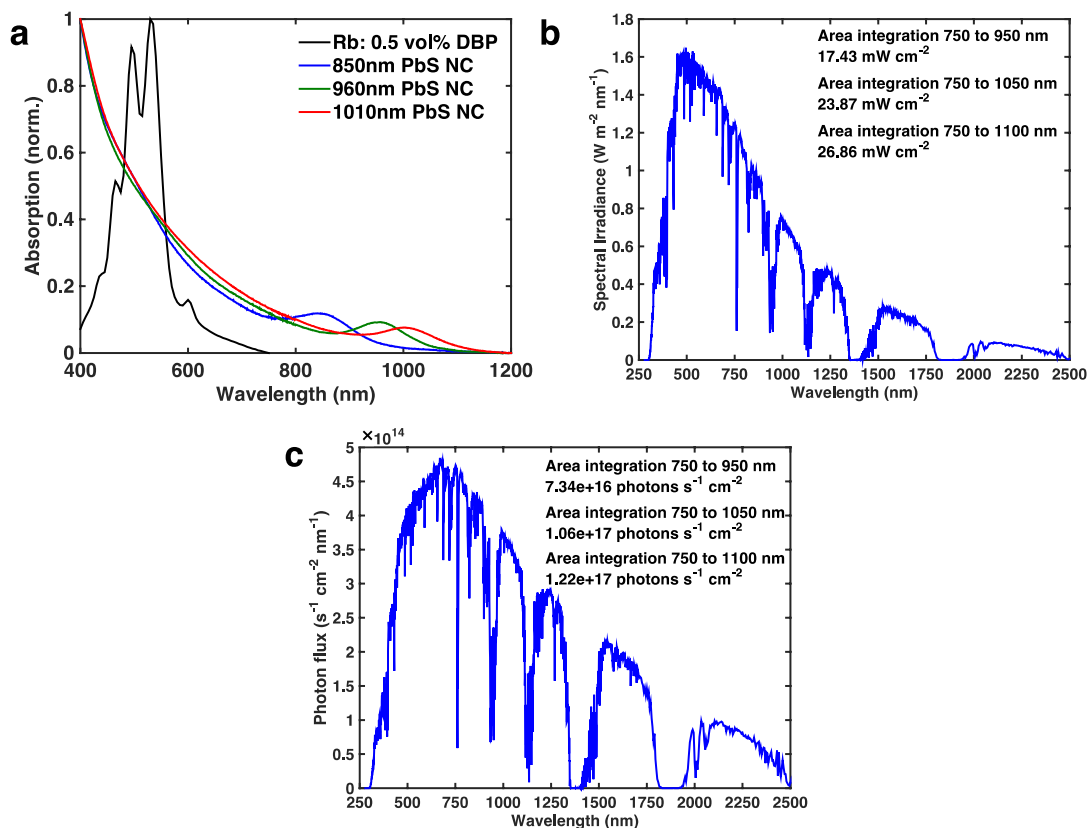


Figure S8. (a) Normalized absorption spectra of rubrene with 0.5 vol% of DBP, $\lambda = 850$ nm, 960 nm, and 1010 nm PbS nanocrystals (NCs). (b) Spectral irradiance of the AM 1.5 solar spectrum. (c) Photon flux per unit wavelength of the AM 1.5 solar spectrum. Area integrations are performed for wavelengths from the absorption tail of the organic to the absorption tail of the respective NCs to obtain the available power density and photon flux potentially harvested by the NCs under one-sun excitation.

References

1. Zhao, N. *et al.* Colloidal PbS quantum dot solar cells with high fill factor. *ACS Nano* **4**, 3743–3752 (2010).
2. Chang, L.-Y., Lunt, R. R., Brown, P. R., Bulović, V. & Bawendi, M. G. Low-Temperature Solution-Processed Solar Cells Based on PbS Colloidal Quantum Dot/CdS Heterojunctions. *Nano Lett.* **13**, 994–999 (2013).
3. Zhou, J., Liu, Q., Feng, W., Sun, Y. & Li, F. Upconversion Luminescent Materials: Advances and Applications. *Chem. Rev.* **115**, 395–465 (2015).
4. de Mello, J. C., Wittmann, H. F. & Friend, R. H. An Improved Experimental Determination of External Photoluminescence Quantum Efficiency. *Adv. Mater.* **9**, 230 (1997).
5. Semonin, O. E. *et al.* Absolute Photoluminescence Quantum Yields of IR-26 Dye, PbS, and PbSe Quantum Dots. *J. Phys. Chem. Lett.* **1**, 2445–2450 (2010).
6. Piland, G. B., Burdett, J. J., Kurunthu, D. & Bardeen, C. J. Magnetic Field Effects on Singlet Fission and Fluorescence Decay Dynamics in Amorphous Rubrene. *J. Phys. Chem. C* **117**, 1224–1236 (2013).
7. Ma, L. *et al.* Fluorescence from rubrene single crystals: Interplay of singlet fission and energy trapping. *Phys. Rev. B* **87**, 201203 (2013).
8. Yost, S. R. *et al.* A transferable model for singlet-fission kinetics. *Nature Chem.* **6**, 492–497 (2014).
9. Jorgensen, W. L., Maxwell, D. S. & Tirado-Rives, J. Development and Testing of the OPLS All-Atom Force Field on Conformational Energetics and Properties of Organic Liquids. *J. Am. Chem. Soc.* **118**, 11225–11236 (1996).
10. Schapotschnikow, P., Hommersom, B. & Vlugt, T. J. H. Adsorption and Binding of Ligands to CdSe Nanocrystals. *J. Phys. Chem. C* **113**, 12690–12698 (2009).
11. Kowalczyk, T., Yost, S. R. & Voorhis, T. Van. Assessment of the Δ SCF density functional theory approach for electronic excitations in organic dyes. *J. Chem. Phys.* **134**, 054128 (2011).
12. Xu, F. *et al.* Efficient exciton funneling in cascaded PbS quantum dot superstructures. *ACS Nano* **5**, 9950–9957 (2011).
13. Akselrod, G. M. *et al.* Visualization of exciton transport in ordered and disordered molecular solids. *Nature Commun.* **5**, 3646 (2014).

14. Kondakov, D. Y., Pawlik, T. D., Hatwar, T. K. & Spindler, J. P. Triplet annihilation exceeding spin statistical limit in highly efficient fluorescent organic light-emitting diodes. *J. Appl. Phys.* **106**, 124510 (2009).